



Contents lists available at ScienceDirect

Journal of the Mechanics and Physics of Solids

journal homepage: www.elsevier.com/locate/jmps

Multi-scale modeling and mechanical performance characterization of stingray skeleton-inspired tessellations

A.K. Jayasankar^{a,f}, R. Seidel^{a,b}, A. Hosny^{c,d}, J.C. Weaver^c, P. Fratzl^a, J. Chen^e, M.N. Dean^{a,*}

^a Department of Biomaterials, Max Planck Institute of Colloids and Interfaces, Am Mühlenberg 1, 14476 Potsdam, Germany

^b Center for Molecular Bioengineering, B CUBE, Tatzberg 41, 01307 Dresden, Germany

^c Wyss Institute for Biologically Inspired Engineering, Harvard University, 02138 Cambridge, United States

^d Dana-Farber Cancer Institute, Harvard Medical School, Cambridge, 02215, United States

^e College of Engineering, Mathematics and Physical Sciences, University of Exeter, Exeter, United Kingdom

^f HP NTU Digital Manufacturing Corporate Lab, Nanyang Technological University, 50 Nanyang Ave, 639798 Singapore



ARTICLE INFO

Article history:

Received 23 July 2019

Revised 15 December 2019

Accepted 13 February 2020

Available online 17 February 2020

Keywords:

Tesserae

Biocomposite

Cartilage

Tunable materials

Hierarchical materials

ABSTRACT

Sharks and rays have distinctive skeletons among vertebrate animals, consisting primarily of unmineralized cartilage wrapped in a surface tessellation of minute polygonal tiles called tesserae, linked by unmineralized collagenous fibers. The discrete combination of hard and soft tissues is hypothesized to enhance the mechanical performance of tessellated cartilage (which performs many of the same functional roles as bone) by providing either rigidity or flexibility, depending on the nature of the applied load. These mechanisms and the effect of tesserae ultrastructure on cartilage mechanics, however, have never been demonstrated in the actual tissue, nor in bio-accurate models. Here, we develop bio-inspired three-dimensional tesserae computer models, incorporating material properties and ultrastructural features from natural tessellated cartilage. The geometries of ultrastructural features were varied parametrically, and the effective modulus of whole tesserae was evaluated using finite element analysis to determine the roles of ultrastructural features in mechanics. Whereas altering some structural features had no effect on the macroscopic in-plane modulus of tesserae, a three-fold increase in the contact surface area between two adjacent tesserae increased the effective modulus of tesserae by 6%. Modeled stress distributions suggest that tesseral 'spokes' (distinct hypermineralized features in tesserae) bear maximum stresses in the skeleton and serve to funnel stresses to particular populations of cells in tesserae, while spokes' lamellated structure likely helps dissipate crack energy, making tesserae more damage-tolerant. Simulations of multi-tesseral arrays showed that maximum stresses in tension and compression are borne by different tissues, supporting hypotheses of multi-functional properties of tessellated cartilage. Further, tesseral array models showed that minor alterations to tesserae/joint shape and/or material properties can be used to tune the mechanical behavior of the whole tiled composite. Our models provide the first functional understanding of the distinct morphologies of spokes and of 'stellate' tesserae (a tesseral shape observed first over 150 years ago), while also being useful drivers for hypotheses of growth, mechanics, load management, and the prevention and 'directing' of cracks in tessellated cartilage, as well as other biological composites. Additionally, these results establish guidelines and design principles for bio-inspired, tunable tiled materials.

© 2020 Elsevier Ltd. All rights reserved.

* Corresponding author.

E-mail address: mason.dean@mpikg.mpg.de (M.N. Dean).

1. Introduction

The skeletal systems of sharks and rays (elasmobranch fishes) consist primarily of unmineralized cartilage (Dean et al., 2009; Kemp and Westrin, 1979; Seidel et al., 2019a), a skeletal tissue far less stiff than bone (Wegst and Ashby, 2004). Unlike mammalian cartilage, elasmobranch cartilage is wrapped with a layer of minute, mineralized, polygonal tiles called tesserae, forming a surface shell (see Fig. 1A-D) (Clement, 1992; Dean et al., 2015, Dean et al., 2009; Kemp and Westrin, 1979; Seidel et al., 2019a). The composite nature of tessellated cartilage is hypothesized to enhance the mechanical properties of the unmineralized cartilage, particularly through the combination of soft and hard tissues in distinct geometric configurations (reviewed in Seidel et al., 2019a), but this has never been demonstrated unequivocally. Tesserae are linked by unmineralized, collagenous joint fibers (see Fig. 1F, H), which, when the skeleton is under tension, are predicted to allow tesserae to pull apart, loading the fibers primarily (Fratzl et al., 2016; Seidel et al., 2017a). In contrast, under compression the hard tesserae are expected to come into contact, resulting in local skeletal stiffening (Fratzl et al., 2016; Liu et al., 2014, 2010). In this way, tesserae and their tissue associations are believed to allow tessellated cartilage to be either flexible or rigid, depending on the nature of the applied loads (Fratzl et al., 2016; Liu et al., 2014, 2010; Seidel et al., 2019a).

The role of the distinct tessellation in load management in shark and ray cartilage has been explored using both physical and computational methods, typically at two disparate size scales: either investigations of whole skeletal elements that disregard the tessellated nature of the mineralized layer or investigations of the interactions of individual tesserae, largely ignoring more macroscopic geometry of the skeleton. The larger-scale, physical experiments have used mechanical testing techniques like flexural bending, and tension and compression tests to confirm that tesserae add rigidity to the cartilage (Balaban et al., 2014; Liu et al., 2014; Macesic and Summers, 2012; Wilga et al., 2016). This is further supported by morphological studies, which show tesserae tend to be thicker in regions where high stresses are predicted to occur (e.g. Balaban et al., 2014; Dean et al., 2017; Seidel et al., 2016; Wilga et al., 2016), with some species even exhibiting multiple layers of tesserae (Dean et al., 2017; Dingerkus and Seret, 1991; Seidel et al., 2017b; Summers, 2000; Summers et al., 2004).

In contrast, our understanding of the smaller scale, mechanical behaviors and interactions of tesserae is less developed. This lack is largely due to the inherent technical difficulties in subjecting tesserae to mechanical tests, a function of their small size (typically ≤ 500 μm wide, with their joints ≤ 2 μm at their narrowest; Fig. 1E and F), complex internal structure, and covering by a fibrous layer (perichondrium) (Dean et al., 2009; Seidel et al., 2017a, 2016). As a result, computational/analytical models have been most helpful in predicting form-function relationships at smaller size scales in tessellated cartilage. For example, a simplified analytical model of the tessellated cartilage cross-section predicted that during compression, stresses will tend to be concentrated in the tessellated layer rather than the unmineralized cartilage (Liu et al., 2010). This hypothesized 'stress-sink' behavior for tesserae was also supported by larger scale computational structural analyses performed on models derived from CT scans of shark jaws and simulating biological loading conditions (Ferrara et al., 2011; Wroe et al., 2008). One of these models also showed that stresses would tend to be lower in jaws composed of tessellated cartilage as compared to jaws modeled in bone, although tissue strains were predicted to be higher (Wroe et al., 2008). Lastly, in the only study to examine the mechanical effects of tesserae properties on the mechanics of the tessellated cartilage composite, parametric, 2D analytical models of tesserae demonstrated that variations in tesserae geometry and material properties should translate into differences in effective modulus of the composite at larger scales, suggesting that emergent skeletal properties can be tuned through local structural/material variations at the tesseral level (Jayasankar et al., 2017).

Computational studies have therefore been important in predicting the role of tesserae in the management of stress, beyond simply providing rigidity to the underlying unmineralized cartilage. However, all smaller-scale studies of tessellated cartilage mechanics have relied on extremely simplified models of tesserae, which were only two-dimensional. Moreover, all previous models assumed tesserae to be materially homogeneous, whereas our recent study showed that tesserae are not simply solid blocks, but rather exhibit complex three-dimensional ultrastructures and local material variations (Fig. 1E, F; see description in Methods below) (Seidel et al., 2016).

In order to better capture the fine-scale mechanics of tessellated cartilage, the current work employs 3D computer models that incorporate high-resolution ultrastructural and material information obtained from analyses of tessellated cartilage from the round stingray, *Urobatis halleri* (Seidel et al., 2016). Through parametric computer modeling, biologically relevant ultrastructure and material property variations were simulated and the resultant computational models subjected to finite element analysis (FEA). This allowed evaluation of stress patterns occurring within tesserae during loading, to determine the effects of various tesserae ultrastructural features on their mechanical performance.

2. Methods

The mineralized tessellated layer was modeled at two length scales (see Fig. 2), described in detail below. In a "local" model (see Fig. 2C), we investigated the effect of ultrastructural variation on stress distribution and the effective modulus of individual tesserae (i.e. not including joint material). In the larger scale "global model," we constructed a tessellated array, containing monolithic tesserae with material properties determined from the local model and also incorporating joint material between tesserae (see Fig. 2D). This allowed investigation of how local, within-tesserae features relate to the material behavior of the tessellated assembly. Both the local and global tesserae models were constructed in a commercial computer-aided design (CAD) package, Rhinoceros 3D Version 5 (Robert McNeel & Associates, Barcelona, Spain), coupled

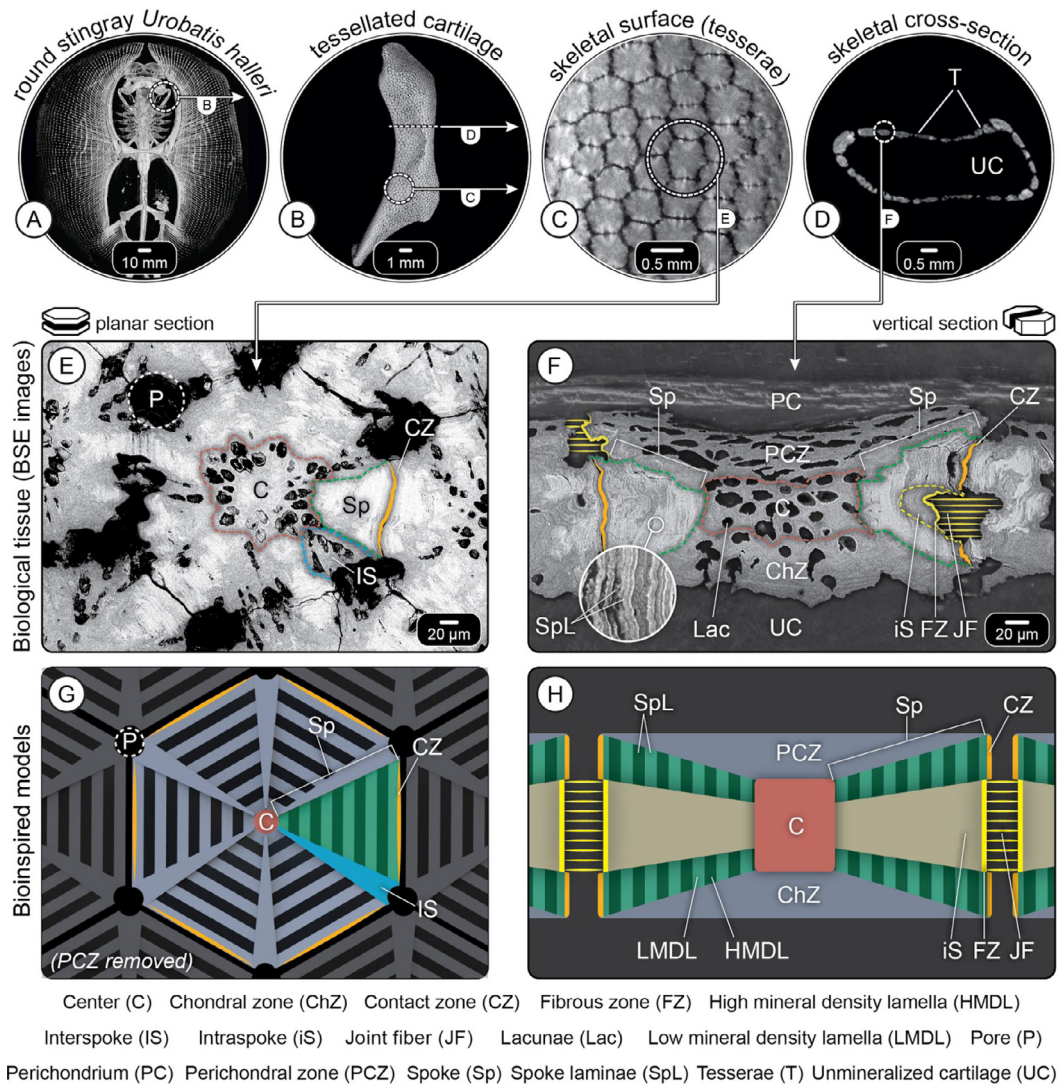


Fig. 1. Tesselated cartilage of stingrays. The skeletal elements of sharks and rays (A and B) are covered with thousands of mineralized tiles, called tesseræ, roughly hexagonal in surface view (C) and rectangular in transverse cross-section (D). A planar section through the tesselal mat (E) and a vertical cross-section of a tessera (F), illustrate their diverse ultrastructural components and the joint fibers connecting adjacent tesseræ. Corresponding translation sketches of planar and vertical cross-sections are shown in (G) and (H), respectively, with abbreviations (used in all figures) listed at the bottom of the figure. Note that the perichondral zone (PCZ) is removed in (G) so that the spokes (Sp) are visible. A–D: MicroCT images; E–F: Backscatter electron microscopy images. Note that these techniques only visualize hard tissues (tesseræ) here and not fibrous tissues, such as the joint fibers between tesseræ. [The reader is referred to the web version of this article, where tesselal regions are color-coded to facilitate interpretation.]

with Grasshopper 3D (v. 0.9.0076), a plug-in for algorithmic programming that allowed ultrastructural features to be varied parametrically (see below).

2.1. Local model: parametric modeling of tesseræ ultrastructure

2.1.1. Natural ultrastructure

Tesseræ are polygonal, mineralized tiles that are predominantly six-sided (i.e. bordered by six neighboring tesseræ) (Baum et al., 2019) and are typically wider than they are thick (Dean et al., 2009; Jayasankar et al., 2017; Seidel et al., 2016). As such, they can be considered roughly hexagonal when sectioned in the plane of the tesselal mat (planar section: Fig. 1E, G) and rectangular in transverse cross-sections of the skeleton (vertical section: Fig. 1F, H). Tesseræ exhibit several distinct structural regions, the arrangements and structural features of which acted as guides for our model construction. The following summary of tesseræ ultrastructure is synthesized from numerous works, which focused predominantly on tesseræ from the stingray *Urobatis halleri* (Dean et al., 2010, Dean et al., 2009; Seidel et al., 2019, 2017a, 2016). Available evidence, however, indicates that these structural features of tesseræ are universally present among different species, although

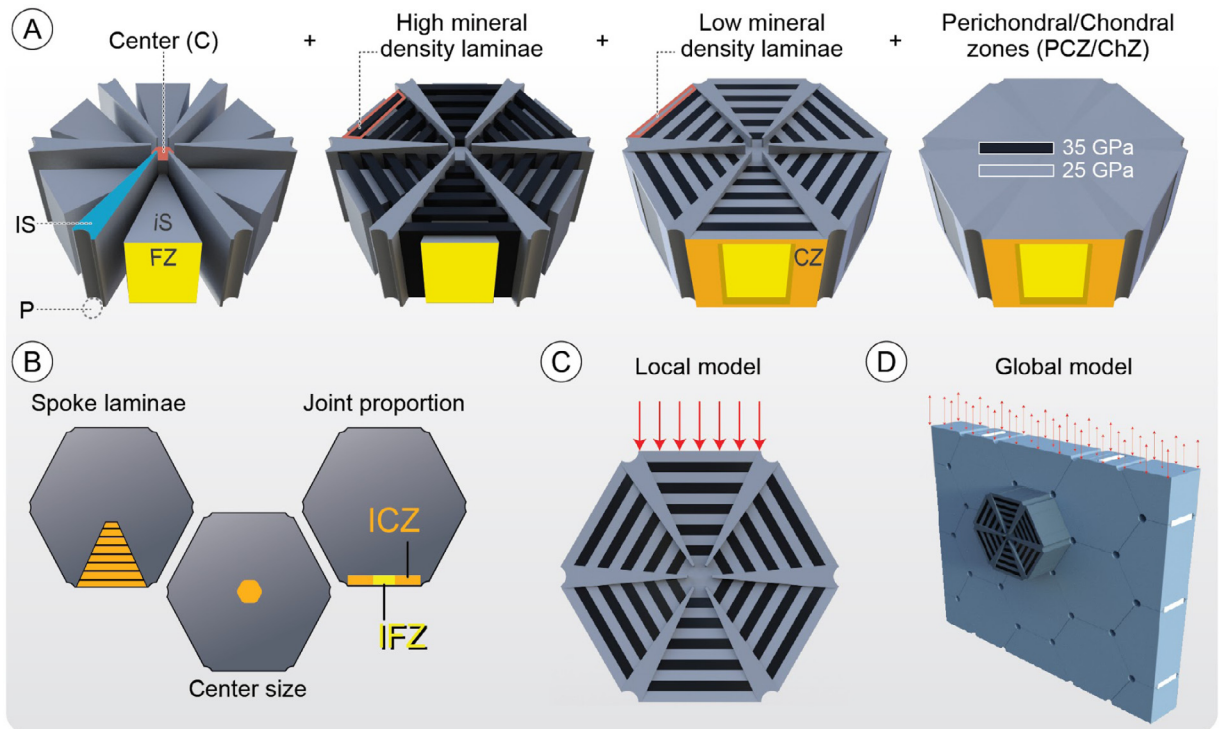


Fig. 2. Multiscale models constructed in this study. A) Step-wise construction of tesseral ultrastructure, assigning biologically-relevant material properties; color-coding and abbreviations are the same as Fig. 1. B) Ultrastructural factors (lamina number, center radius and contact surface area) varied parametrically in the local model, to derive their effect on net effective stiffness of tesserae. C) Local model (single tessera, including ultrastructural features); note that the perichondral zone (PCZ) has been removed, as in Fig. 1G. D) Global model (multi-tesserae array), where tesserae are assigned a homogeneous material property, derived using the local model (see text). [For interpretation of the references to color in this figure, the reader is referred to the web version of this article.]

their dimensions/proportions vary (Seidel et al., 2016). Anatomical terminology, abbreviated in italics below, is illustrated in Fig. 1 and used throughout the figures.

The tesseral center region (C: Fig. 1E-H) occupies the approximate center of mass of the tessera. Extending outward from the center are the ‘spokes’ (Sp: Fig. 1E-H): high mineral density wedges, radiating from the center toward the joints with adjacent tesserae. Intervening between spokes are wedge-shaped ‘interspoke’ (between spoke) regions (IS: Fig. 1E, G), which have a lower mineral density than spokes and about the pores (P: Fig. 1E, G) at the vertices of some tesserae, rather than the joint surfaces at the tesseral sides. The alternating pattern of spoke and interspoke regions pinwheeling around the tesseral center resembles spokes on a wheel in planar sections (see Fig. 1E, G). Spokes are characterized by the presence of thin plate-like lamellae (2–3 μm) arranged parallel to the tesseral joint surface. Spoke laminae (SpL) alternate between higher and lower mineral density lamellae (HMDL, LMDL), giving the spokes a banded appearance in backscatter electron imaging and high-resolution microCT. In vertical sections, spokes often enclose a pyramidal ‘intraspoke’ (within spoke) region (iS: Fig. 1F, H), comprised of lower mineral density material (similar to interspoke regions) and also bordering the joint space between tesserae. Between the center region and the outer fibrous perichondrium (PC: Fig. 1F) is the perichondral zone of the tessera (PCZ: Fig. 1F, H), and between the center and underlying unmineralized cartilage (UC: Fig. 1F) is the chondral zone of the tessera (ChZ: Fig. 1F, H), both zones with mineral densities similar to inter- and intraspoke regions. All non-spoke regions within tesserae (i.e. center, interspoke, intraspoke, perichondral and chondral regions) are perforated by prolate spheroidal cavities (*Lac*: lacunae, 15–20 μm long, 5–10 μm in diameter), which contain cells and unmineralized matrix (Chaumel et al., 2020; Dean et al., 2009).

The joints between tesserae are anatomically complex (see Fig. 3) and deserved careful consideration from a modeling perspective. The edges of tesserae, which border the joint space, are comprised of two anatomical regions with distinct morphologies and tissue associations (Fig. 1E-H and Fig. 3A). Where neighboring tesserae come into physical contact, there is a largely flat “contact zone” (CZ: Fig. 1E-H), always associated with and flanked by spokes in the tessera. In contrast, the “fibrous zones” (FZ: Fig. 1E-H), where collagen joint fibers (FB) tether neighboring tesserae to one another, are recessed and flanked by intraspoke tissue in the tessera. The morphologies and interactions of these two zones on the joint face of a tessera are elaborate, with fibrous and contact zones interweaving considerably (see Fig. 3). However, the flanking of contact zones by spoke material and of fibrous zones by non-spoke material appears to be a diagnostic feature of tesserae (Seidel et al., 2019, 2016).

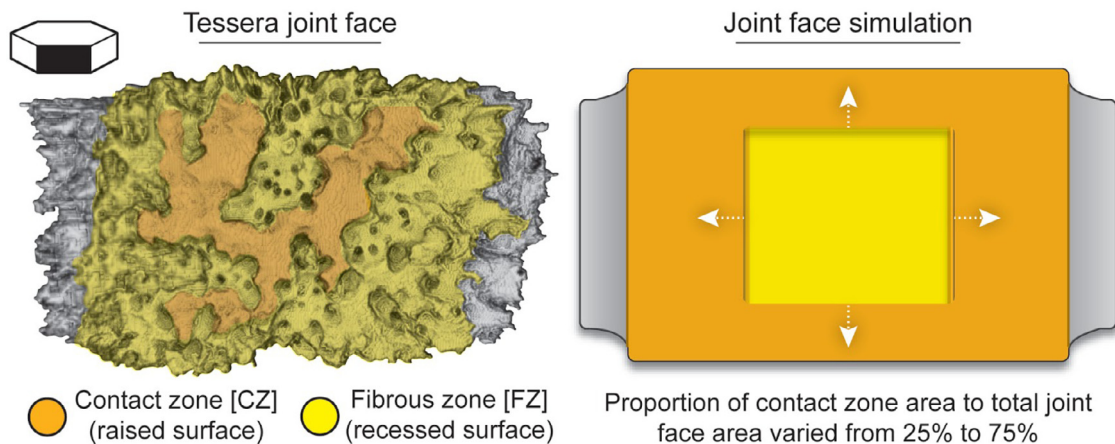


Fig. 3. Biological structure (left: pseudocolored microCT image) and corresponding model (right) of the complex tesseral joint face. Both images show a lateral, 'neighbor's eye' view of a tessera. The joint face in *U. halleri* tesserae comprises a flattened, raised region where neighboring tesserae are in contact (contact zone) and a recessed zone where fibrous tissue links neighboring tesserae (fibrous zone). The proportion of the joint face occupied by the contact and fibrous zones is reciprocal and in the constructed local model, this could be changed parametrically. Color coding is the same as Figs. 1 and 2; compare with those figures and note that the contact zone is associated with spokes (Sp), whereas the fibrous zone is associated with the intraspoke region (iS). [For interpretation of the references to color in this figure legend, the reader is referred to the web version of this article.]

Table 1

Ultrastructural features, their dimensions, and their proportions with respect to tesserae dimensions (i.e. the fibrous zone is ~40% of tesserae width and ~60.5% of tesserae height). Ultrastructural dimensions are derived from previous anatomical descriptions of tesserae from the stingray *Urobatris halleri* (see text).

Tesserae (<i>T</i>)	width: 448 μm	height: 200 μm
Fibrous zone (<i>FZ</i>)	width: 180 μm 40%	height: 121 μm 60.5%
Contact zone (<i>CZ</i>)	width: 218 μm 48%	height: 200 μm 100%
Center (<i>C</i>)	radius: 20 μm 4%	height: 155 μm 77%
Spoke (<i>Sp</i>)	height at center: 155 μm 77%	height at edge: 200 μm 100%

2.2. Local model construction

In the local model, a single tessera was modeled as a hexagonal block, with geometries and dimensions of tesseral ultrastructures modeled according to those observed in the stingray *Urobatris halleri* (see Table 1) (Dean et al., 2009; Seidel et al., 2019, 2016). The different ultrastructural regions (e.g. spoke, interspoke regions) were modeled as separate pieces and then assembled together to form the complete, integrated tessera (see Fig. 2A). This assembly process facilitated the parametric variation of the dimensions and properties of individual ultrastructural features. We describe the arrangement of features and their assembly below, including the same anatomical abbreviations listed in the paragraph above, to facilitate reference to Figs. 1 and 2.

The tesseral center (*C*) was modeled as a polygon at the geometric center of the tessera, with wedge-like spoke (*Sp*) and interspoke (*iS*) regions radiating from its vertices towards the outer edges of the tessera (see Fig. 2A). To accommodate the intraspoke (*iS*) region (described below), spokes were modeled with an internal, pyramid-shaped cavity, with the base at the tesseral edge and the tip extending toward the tesseral center. Spokes were divided into laminae of equal thickness parallel to the joint face. Laminae were assigned high or low moduli in alternating order to mimic the banding pattern of alternating high/low mineral density laminae (*HMDL*, *LMDL*) and material properties observed in *U. halleri* tesserae (see Fig. 1F) (Seidel et al., 2019). Both the first lamina near the center and the last lamina at the joint face were assigned the lower modulus, mimicking the biological condition where newly deposited material at tesseral edges has a lower mineral content (Seidel et al., 2019). Semi-circular cavities were hollowed out at the tesseral vertices (i.e. the distal ends of the interspoke regions), to mimic the pores (*P*) often observed at the intersection points of multiple tesserae in natural tessellations (Fig. 1E, G) (Maisey, 2013; Roth, 1911; Seidel et al., 2016; Chaumel et al., 2020). The tessera model was completed by adding the perichondral and chondral zones (*PCZ*, *ChZ*) on the top and bottom of the tessera, respectively. The addition of these regions creates the planar surfaces of the top and bottom of the model (compare the 3rd and 4th images in Fig. 2A). The small, spheroidal cavities (cellular lacunae; Fig. 1F), typically present in all non-spoke regions in tesserae, were not modeled, as the 3D structure and material properties of these cavities and their tissues have not yet been described.

The distal end of the intraspoke region (i.e. abutting the joint) was recessed relative to that of the spoke region in order to create a simplified joint surface. This captured the primary structural characteristics of the joint face (see Fig. 3), while facilitating efficient finite element analysis. In our local model, the distal end of the spoke (i.e. the lamina at the intertesseral joint-end of the spoke) served as the contact zone surface where tesserae come into contact (*CZ*: orange region

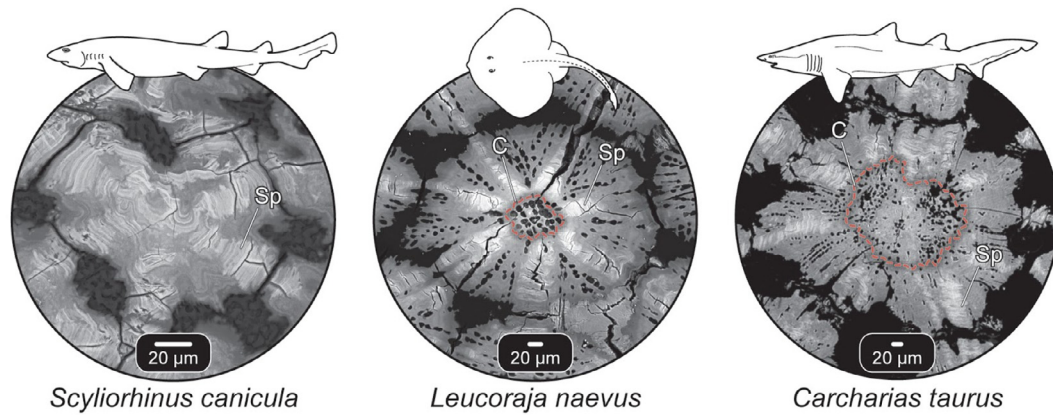


Fig. 4. Natural variation of tesseral ultrastructural features in several elasmobranch species (two sharks and a skate). Note the variation in the size of the center region (C; outlined in red), the predominance of spokes (Sp), and the cellularity of the tesserae (the black holes in tesserae are lacunar spaces, where cells are housed in life). Note also the difficulty in delineating the center region for *Scyliorhinus*, where the round lacunae typically diagnostic for this region appear to be absent [For interpretation of the references to color in this figure legend, the reader is referred to the web version of this article.]

in Figs. 2A, 3), whereas the distal end of the intraspoke region formed a recessed and rectangular fibrous zone (FZ: yellow region in Figs. 2A, 3). In this way, as in the biological system, the contact and fibrous zones were modeled as distinct, but closely associated regions, flanked by different materials (i.e. contact zones flanked by spokes, fibrous zones flanked by intraspoke regions). In the ‘global model’ described below, which models a full tessellation, fibrous joint material is fully bonded to the intraspoke regions to connect tesserae to their neighbors.

2.3. Ultrastructural variations in tesserae

To investigate the effects of ultrastructure on performance (tesserae rigidity and intratesseral stress distribution), three key ultrastructural features were varied in the parametric local (single-tessera) models (see Fig. 2B): 1) the number of laminae in a spoke, 2) the size of the center region (center radius), and 3) the area of the contact zone surface in proportion to the fibrous zone surface. These three ultrastructural variables were chosen to represent the natural variation in tesseral ultrastructure previously observed among different species of elasmobranchs (see Fig. 4) (Seidel et al., 2016). The morphologies of the selected ultrastructural features were varied through a wide range that included morphologies previously observed for tesserae of the stingray *U. halleri* (see Table 1; natural character states are marked in red in Fig. 5).

2.3.1. Varying lamina number

Tesserae increase in size as the animal grows, apparently via deposition of new material at their margins (e.g. on contact zone surfaces) (Dean et al., 2009; Seidel et al., 2016). Through this process, new laminae (of relatively consistent thickness; Seidel et al., 2019) are added to spokes and spokes increase in length with animal age. As a result, for modeling purposes, the thickness of laminae relative to spoke length can be considered to vary. In our model, spokes were evenly sub-divided along their primary axes to form laminae, the number of which could be altered. Laminae were of equal thickness, but the wedge-like shape of spokes meant that laminae decreased in volume from edge to center.

In *U. halleri* tesserae, spoke laminae are ~1.5–3.5 µm thick (Seidel et al., 2019). The model mimicking this morphology (containing 151 laminae in each spoke, with each ~1 µm thick) was extremely computationally expensive and so all additional models compared to test the effect of lamina number contained fewer laminae (51, 21, 15, 11 laminae). These chosen values for lamina number were all odd in order to maintain the presence of soft laminae at the outer rim and adjacent to the center. To optimize computational resources, no additional models were tested with more than 51 laminae and fewer than 151 laminae, since lamina number was shown to have little effect on tesserae properties (see Results).

2.3.2. Varying center size

In the natural system, across species and across age, the proportion of tesseral diameter occupied by the center region is variable (see Fig. 4) (Seidel et al., 2016). In our model, because interspoke and spoke regions were linked to the center region, changes in center diameter resulted in concomitant inverse changes in the length/volume of interspoke and spoke regions (i.e. a larger center resulted in shorter spokes). To investigate the mechanical effect of different center sizes, the diameter of the center was varied from 90, 25, 20 to 15 µm (~40%, 10%, 8% and 6% of tesseral diameter). Tiles with centers 20 µm in diameter (~8% of tesserae diameter) were the most biologically relevant models (with regard to *U. halleri* tesserae; Seidel & Dean, pers. obs.).

2.3.3. Varying contact zone area

The complex physical interactions of adjacent tesserae at their joints are expected to play an important role in tessellated cartilage mechanics (Baum et al., 2019; Fratzl et al., 2016; Seidel et al., 2016). In our models, each joint face is comprised

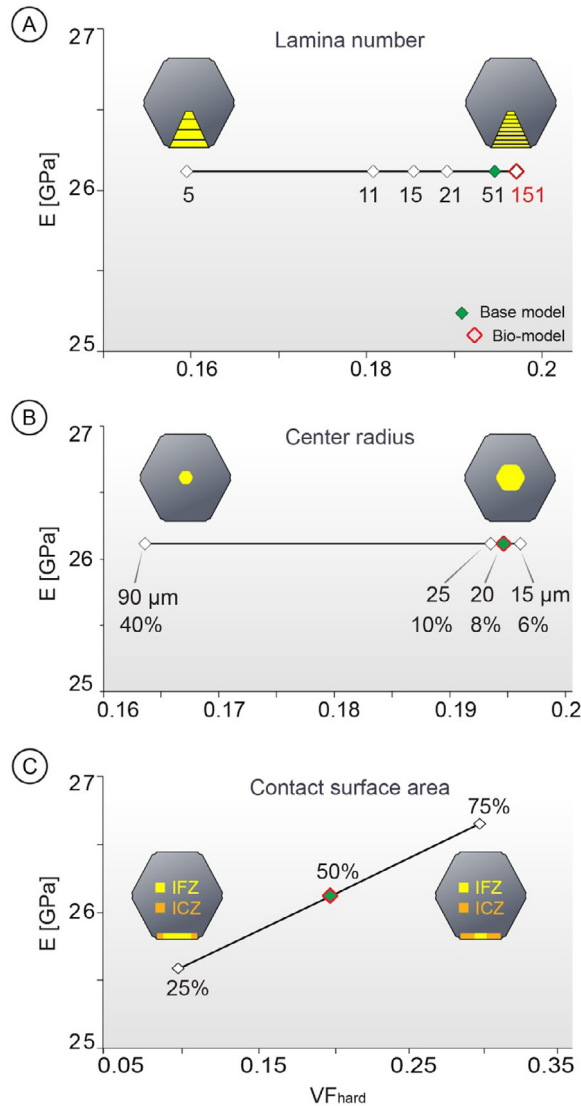


Fig. 5. Effect of varied ultrastructure (lamina number, center radius and contact surface area) on the volume fraction of hard material relative to tesserae volume (VF_{hard} : x-axis) and effective modulus (E : y-axis) A) The lamina number varied from 5–151 laminae. B) The radius of the center varied from 90 μm to 15 μm . C) The contact surface area varied from 25%–75% of the joint surface. Note that the modeled ultrastructural changes had little effect on the net effective stiffness of the tessera, except in the 'contact surface area' model, where stiffness increased by 6% with the three-fold increase in contact surface area. Green-filled points indicate the 'base model' and red-outlined points represent the 'bio model.' [For interpretation of the references to color in this figure legend, the reader is referred to the web version of this article.]

of a reciprocal combination of contact zone and fibrous zone area. To investigate the effect of this interaction on tesserae rigidity, the contact zone area was varied in proportion to the fibrous zone area, from 25%, 50% to 75%. A contact zone proportion of 50% was the most biologically relevant (with regard to *U. halleri* tesserae; Seidel & Dean, unpublished data). As spoke and intraspoke regions are associated in our models with the contact and fibrous zones, respectively, increase in contact zone area resulted in a concomitant increase in spoke volume, a decrease in fibrous zone area and a decrease in intraspoke volume.

2.4. Finite element analysis

Two versions of the local model were used to address the contribution of individual structural and compositional features to tesserae mechanics (Table 2). The model versions differed only slightly: the "bio model" exhibited ultrastructural features most similar to *U. halleri* tesserae (151 laminae, 20 μm center, 50% contact area), whereas the "base model" was a simplified version of the bio model, with the same dimensions and features, but only 51 laminae. The base model required considerably

Table 2

Variations on the local model used for finite element analysis (FEA). The Base model and Bio model are defined in the top rows of the table; these models differed only in lamina number. The Base model was used when possible to reduce analysis time. In the subsequent rows of the table, the models used for each FEA experiment are listed, as well as figures showing relevant results. For experiments where ultrastructure was varied parametrically, morphological iterations are listed. Relevant Base and Bio model values are indicated by single and double asterisks, respectively.

Structural features	Base model (*)	Bio model (**)
No. of laminae	51	151
Center radius	20 μm	20 μm
Contact surface area	50%	50%
Variables tested		
Lamina number (Fig. 5)	5, 11, 15, 21, 51*, 151**	
Center radius (Fig. 5)	90, 25, 20*, 15 μm	
Contact surface area (Fig. 5)	75%, 50%*, 25%	
Maximum stress (Fig. 6)	(Bio model used)	
Strain energy density (Fig. 7)	(Bio model used)	
Stress in spokes (Fig. 9)	0, 5, 21, 151** laminae	

less computational power as a result of its fewer laminae; this time-saving modification was used where possible, because lamina number was shown to have little effect on tesserae properties (see Results). Table 2 outlines which model version was used in which experiment: The bio model was used to investigate stress distribution and overall performance of tesserae ultrastructures during loading, whereas the base model was used to study the effects of ultrastructural feature variation on tesserae rigidity (e.g. center radius or contact surface area). Further, both base and bio models were used to investigate the effects of lamina number variation on tesserae rigidity.

The models listed in Table 2 (including all parametric iterations for each of the three chosen ultrastructural features) were constructed and exported from Rhinoceros in SAT file format into a finite element analysis package (ABAQUS Version 6.13 Dassault Systèmes, Waltham USA). All components shown in Fig. 2A were modeled as fully bonded with each other. The models were meshed with 10-node quadratic tetrahedral elements (C3D10). After a mesh sensitivity test, where stress variation was tested for seed sizes with degrees of freedom from [3 \times 424,078 nodes] to [3 \times 873,532 nodes], the global seeding size was set at 0.015 μm (Appendix A.1).

In the local model, each tessera ultrastructural feature was assigned linearly elastic properties and a Poisson's ratio of 0.3, a moderate value for mineralized skeletal materials and common for models of biological tissues (Zhang et al., 2013). Mineralized tissue moduli were obtained from a nanoindentation study of stingray tesserae (Seidel et al., 2019). All tesserae ultrastructures were assigned a modulus of 25 GPa except for the hard laminae in the spokes, which were assigned a higher modulus of 35 GPa. The model was constrained at the bottom joint surface and a uniform displacement boundary condition was applied to the top of the model in the y-direction (along the top-bottom axis). The displacement boundary condition simulated an equivalent strain of 1.3%, compressing the tessera in the y-direction.

2.4.1. Mechanical performance assessment

To understand the mechanical role played by each ultrastructural feature, the mechanical behavior of the local model was assessed using several metrics. The maximum stress along the loading direction (σ_{yy}) was quantified in each component (spoke, interspoke, intraspoke, perichondrium and center) of the modeled tessera. Note that the maximum stress in single elements is often not appropriate to represent entire regions (e.g. due to stress singularities), and so to provide a more statistically meaningful perspective on the level of biomechanical stimuli experienced by the tissues, we averaged the stress over the component volume experiencing stresses in the top 10% range of the whole component:

$$\sigma_{yy} = \frac{\sum_{i=1}^n \sigma_{yy}^i \cdot V_i}{\sum_{i=1}^n V_i} \quad (1)$$

where σ_{yy} is the stress component in the y-y loading plane, V_i is the elemental volume with the top 10% of the peak stresses and i represents the element number.

Additionally, the average strain energy density was calculated for loaded tesserae models using the standard ABAQUS output variable identifier, SENNER:

$$\text{Strain energy density} = \frac{\sum_{i=1}^n \text{SENER} \cdot V_i}{\sum_{i=1}^n V_i} \quad (2)$$

Strain energy density (strain energy normalized by volume) is a common measure of energy storage, also approximating the relationship between stress and strain in a structure or material (Sih and Macdonald, 1974). The maximum strain energy density can be used as a proxy for the extremes of material performance, predicting possible failure regions and areas of crack propagation in materials (Fratzl et al., 2007).

Additionally, to evaluate the contribution of ultrastructural variation to whole tessera mechanical behavior (and to facilitate the construction of the global model, see Section 2.2), a single homogenized effective modulus (E_{eff}) for tesserae was calculated from the most biologically relevant, heterogeneous single tessera model (local model). This effective modulus captures in a single value the mechanical contributions of the complex heterogeneous features modeled within the tessera, by assuming the heterogeneous tessera will bear the same energy as a tessera of E_{eff} under the same boundary conditions (Chen et al., 2017):

$$E = \frac{W_{\text{Base model}}}{W_{\text{Homogeneous model}}} \cdot E_{\text{Homogeneous model}} \quad (3)$$

where $W_{\text{Base model}}$ is the elastic strain energy density of the local bio model and $W_{\text{Homogeneous model}}$ is the elastic strain energy density of a tessera of equal volume composed of an arbitrary single material ($E_{\text{Homogeneous model}} = 35$ GPa). To verify that the substitutive material (E_{eff}) accurately mimics the energy storage of the biological model, a tessera comprising only effective modulus material was modeled in ABAQUS and its strain energy density derived as in Eq. (3). The effective modulus of whole tesserae was calculated for each of the 13 varied-ultrastructure models.

Finally, to understand the mechanical role of spoke laminae, the stress at maximum strain was plotted for a transect running through the tessera along the loading axis: starting from the loaded contact surface, traversing the spoke to the tesseral center, and then exiting distally through the contralateral spoke (see Fig. 9). The stress values as a function of position along the path were plotted for four tesserae models: models with 21, 51, 151 laminae and a tessera with a uniform material modulus of 25 GPa (i.e. a model with homogeneous spokes lacking laminae).

2.5. Global model: integration of the local tesserae model into the tesseral matrix

2.5.1. Construction of the global model

A tesseral mat was modeled using Grasshopper and Rhinoceros, by assembling tesserae with the same structural dimensions as the base model into a 3-by-3 array (see Fig. 2D). Tesserae were arranged 1 μm apart from each other and connected to their neighbors using a soft, fibrous joint material projecting from the fibrous zone surface of the intraspoke region (yellow region, Figs. 2A, 3). To facilitate computation, tesserae were modeled as homogeneous (i.e. lacking ultrastructure) and assigned the effective modulus material property ($E_{\text{eff}} = 26.1$ GPa, determined from the homogenization above; see Results). The Poisson's ratio of the tesserae was modeled as 0.3.

The material properties of the biological, fibrous intertesseral joint tissue is unknown, but due to its construction from parallel-aligned collagen fibers (Clement, 1992; Dean et al., 2009; Seidel et al., 2017a) it is hypothesized to be rigid under tension and soft under compression (Fratzl et al., 2016; Seidel et al., 2019a) and therefore highly non-linear. To capture this behavior, we constructed a hypothetical material model using the ABAQUS material library, combining the stress-strain curves of tendon in tension (Maganaris and Paul, 1999) and mucosa under compression (Chen et al., 2015). The 2nd order Ogden hyperelastic material model provided the closest fit to our composite curve and so was used as our intertesseral fiber material (Appendix Table A.2).

The tesseral mat was loaded in both tension and compression while constrained at the bottom surface (see Fig. 2D). Similar to the local base model, a 1.3% uniaxial strain was applied within the plane of the tesseral mat. The stress in the tesseral mat was calculated using Eq. (2) and the stress-strain curves were plotted for both tension and compression. In addition, for comparative purposes and to demonstrate the role of material and structural properties in the mechanics of the tesseral array, three additional models were created where the tesseral mat was modeled with (1) tesserae of lower modulus material (25 GPa), (2) tesserae of higher modulus material (35 GPa), or (3) intertesseral joints that were twice as wide as those in the base global model.

3. Results and discussion

3.1. Local model: Ultrastructural variations

The hexagonal structure of the modeled tessera has a high tolerance to structural changes or defects, as demonstrated by the fact that not all modeled ultrastructural variations produced demonstrable effects on tesseral mechanical performance. The variation in spoke lamina number and center radius, for example, had marginal effects on the effective modulus (E_{eff}) of the tessera, which varied less than 1% across models, remaining ~ 26.1 GPa (see Fig. 5A and B). This lack of change is likely a function of the design constraints of the tessera model (see 2.1 Local model). Higher modulus material (35 GPa) in our model is found only in spokes, the structure of which is not greatly affected by our modeled changes in lamina number or center radius. For example, when the number of laminae was varied from 5 to 151, the volume fraction of hard material (VF_{hard} : volume of higher modulus material relative to whole tessera volume) only increased by 4% (VF_{hard} 5 lamina = 15% vs. VF_{hard} 151 lamina = 19%). This increase in VF_{hard} is not large enough to alter the effective modulus of the tessera. The increase of VF_{hard} with increasing lamina number (see Fig. 5A) is due to the spokes being wedge-shaped structures (in both planar and vertical sections; Figs. 1 and 2). When there are few laminae, spokes are dominated by the material of the outermost lamina (i.e. the lamina with the largest volume). This was lower modulus material

(25 GPa) in our models, constituting ~60% of spoke volume in the 5-lamina model. However, as the number of laminae increases (i.e. laminae became thinner), the volumetric proportion of higher and lower modulus material in spokes converges on 50%.

Similarly, decreasing the center radius size from 40% to 6% of tesserae width had little effect on $V_{F_{hard}}$, which only increased from ~16% to 19% (see Fig. 5B). Although the decrease in center radius increases the radial length of the spokes (which are bound in our model to the vertices of the center region), there is little change in the volume of hard material with respect to whole tesserae volume, and therefore a negligible effect on tesserae effective modulus.

In contrast, change in the contact zone area had a considerable effect on $V_{F_{hard}}$ and, as a result, also the effective modulus of the tessera (see Fig. 5C). The increase in the contact zone area (from 25% to 75%) resulted in $V_{F_{hard}}$ increasing by 20% (0.09 to 0.29). This is also linked to the design constraints of the model, where joint surfaces of tesserae are comprised of reciprocal combinations of fibrous and contact zone areas (see Figs. 2, 3). As a result, an increase in a tessera's contact zone area concomitantly decreased the area of its fibrous zone. In our simulation, the increase of the contact zone area led to an increased volume of the higher mineral density spoke region (flanking the contact zone), and consequently reduced the volume of the lower mineral density intraspoke region (flanking the fibrous zone). Therefore, the overall volume of hard laminae was increased in the tessera model, resulting in an increase in the effective modulus of the tessera by 6% (from 25.1 to 26.6 GPa).

Our modeled ultrastructural variations suggest that structural changes that result in the increase of spoke (i.e. higher mineral density) material in tesserae have the largest effect on tesseral rigidity. As such, the differences in the proportional thickness of spoke laminae and in the size of the center region occurring across species and ages (Seidel et al., 2016) are predicted to have little effect on whole tesseral stiffness. In contrast, alterations that result in changes to the contact zone area should have a pronounced effect on tesseral mechanics. Indeed, Seidel et al. (2016) microCT and backscatter SEM survey of tesserae from several elasmobranch species' implies that the proportion of high mineral density material does vary by species (see Fig. 4), suggesting that changes in spoke volume and contact surface area may be a pathway by which local rigidity is tuned in the tessellated cartilage skeleton.

3.2. Mechanics of the bio-relevant model and its ultrastructure

Individual tesseral ultrastructures exhibit distinct mechanical behaviors, which vary according to their relationship with the axis of loading. This is visible in plots (see Fig. 6A) and FEA models (see Fig. 6B) showing on-axis peak stresses in each component of the bio model as a function of increasing strain, and particularly when structures are separated into those directly in line with load and those not (see Fig. 6A). When the load is applied to the contact surface of the tessera, stress builds up in the on-axis spokes (i.e. those flanking the loaded contact surfaces) and adjacent interspoke regions and radiates towards the center of the tessera (see Fig. 6B). Reaching the end of a loading cycle, these stresses also radiate laterally outward from the center to some degree, to the off-axis regions.

Our models suggest that the ultrastructural features in line with the load, and particularly spokes, will experience maximum stresses, while also acting as channels, ferrying mechanical stimulation to the tesseral center. As a result, the center has the highest strain energy density when compared to other ultrastructural features (see ~0.25 strain in Fig. 6). This is an important observation, considering that whereas spokes are acellular, the center is filled with cells, housed in lacunar spaces and connected by short canalicular passages (see Figs. 1E-F and 7) (Dean et al., 2010; Seidel et al., 2017a, 2016; Chaumel et al., 2020). As mammalian chondrocytes are capable of sensing mechanical signals (Chen et al., 2013; Lammi, 2004; Wann et al., 2012; Wu and Chen, 2000), we hypothesize that the cells in the center region of tesserae act as sensors, collecting mechanical loading information within tesserae. This role may explain the different appearance of chondrocytes in the center of tesserae, which are larger and often rounder in cross section than chondrocytes in surrounding tissues (i.e. in unmineralized cartilage, joints, and tesserae) (Dean et al., 2010; Dean et al., 2009; Seidel et al., 2016; Chaumel et al., 2020), perhaps suggesting a division of labor among the different shaped cells throughout tessellated cartilage. The center region itself does not appear to contribute appreciably to the effective modulus of tesserae (Appendix A.3). Additionally, it should be noted that the stresses in non-spoke/non-center regions (i.e. interspoke, intraspoke, perichondral and chondral regions) are comparatively low during loading, suggesting that by ferrying stresses through the acellular spokes to the center region, spokes protect cells in adjacent regions (Fig. 7).

We tested and supported this hypothesis using an altered version of our CAD tessera model, where non-spoke/non-center regions were assigned negligible mechanical properties, simulating a tessera lacking these regions. The resultant model exhibited nearly the same effective modulus as the complete bio model, arguing that non-spoke/non-center regions may perform a non-mechanical role, perhaps acting as repositories for cells for tissue growth. This also explains the geometries of the non-polygonal, stellate (asterisk-shaped) tesserae, recently described as 'trabecular tessellated cartilage' (Atake et al., 2019) (Fig. 8). Comparing published images from several species and studies (Atake et al., 2019; Fig. 1E in Knötel et al., 2017; Fig. 81 in Leydig, 1857; Fig. 2B in Seidel et al., 2016) with recent data on tesserae ultrastructure (Seidel et al., 2019, 2016), we propose that the stellate morphology of these tesserae is due to a reduction or lack of interspoke regions (Fig. 8B-C). Given our demonstration of the mechanical importance of spokes and the possibility of mechanosensation by center cells, we posit that the stellate morphology represents tesserae stripped down to their mechanical necessities (i.e. just their spoke and center regions); the reason for this 'reduced' morphology requires further investigation.

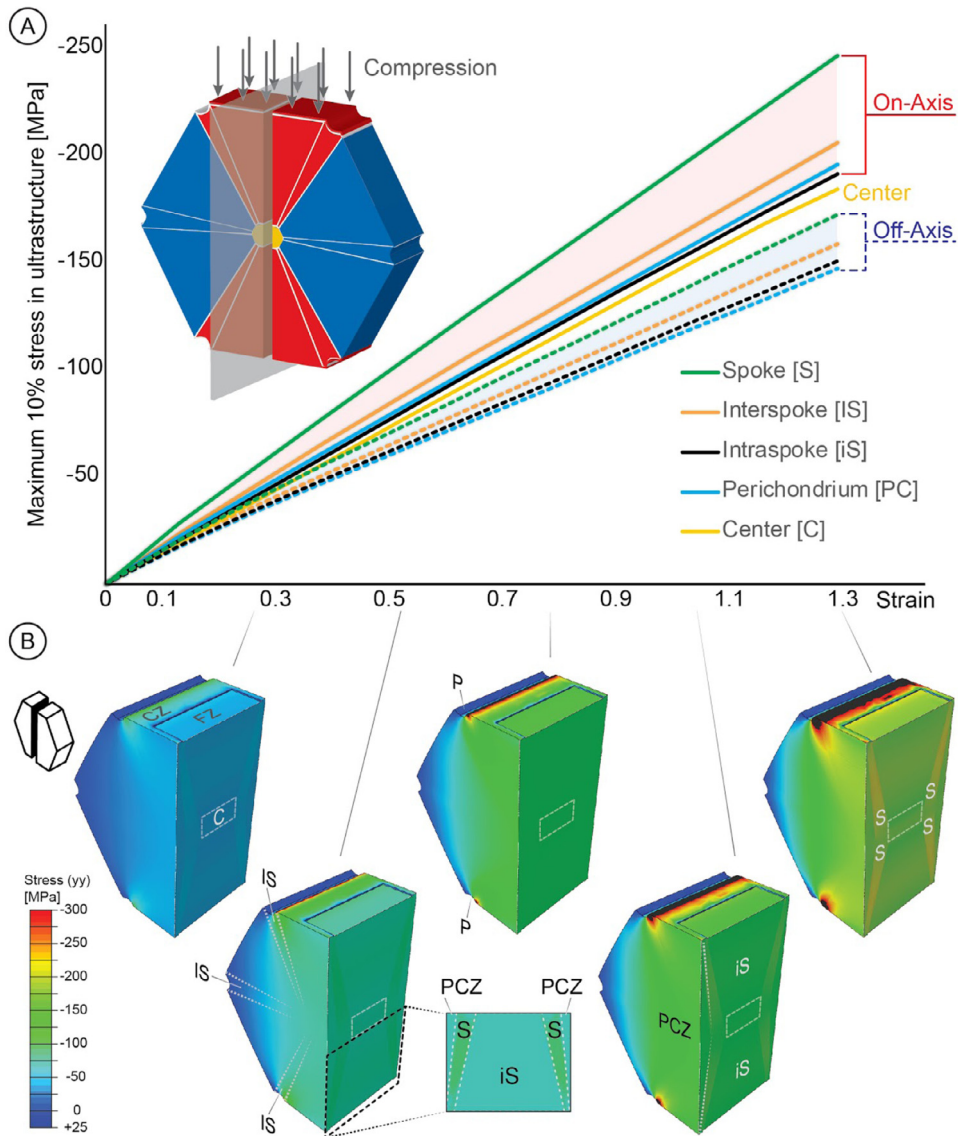


Fig. 6. Stress in the loading direction in the local model (loaded from the top and constrained on its bottom face). A) Plot of maximum 10% stress for each ultrastructural feature in the loading direction (S_{yy}) with respect to strain. The spokes experience maximum stress while transferring the stresses across the tesserella through the center. B) Vertical cross-section of the tesserella showing the stress contours of stress (S_{yy}) in the loading direction. Ultrastructural features are indicated by lines and abbreviations (as in Fig. 1). Note that maximum stresses occur in the on-axis spoke and interspoke regions, radiating from the contact zone (CZ) across the tesserella through the center (C). [The reader is referred to the web version of this article, where color is used to facilitate interpretation.]

In addition to the stresses observed in spokes, notably high stresses are also visible at the corners of the contact surfaces, adjacent to tesserella pores (Fig. 6B). We verified, by comparing the bio model with a similar CAD model lacking pores, that these regions of high stress are largely artifacts (singularities, tending toward an infinite value) due to our method of model construction creating artificially sharp corners bordering pores. It should be noted, however, that tesserella pores are natural features (see Fig. 1E) (Maisey, 2013; Roth, 1911; Seidel et al., 2016; Chaumel et al., 2020) and that holes, edges and corners are common stress concentrators in tissues (Petrie and Williams, 2005). Therefore, it is possible that tesserella pores create a unique stress environment in tessellated cartilage that may stimulate tissue growth.

The mechanical importance of on-axis spokes and their structure is also evident from stress traces plotted along measurement transects running through the tesserella along the loading axis, from the loaded tesserella edge to the constrained edge (see Fig. 9). Comparing a homogeneous model (Appendix A.3) with models with 5, 21 and 151 laminae per spoke, the stress behavior was always similar in contralateral spokes (left and right sides of the graph) under the applied loading conditions, and therefore, all stress line maps were symmetrical around the center. Whereas in the homogeneous (i.e. no laminae) model, stress increased smoothly from the intertesserella contact zone along the spoke to the center, in heteroge-

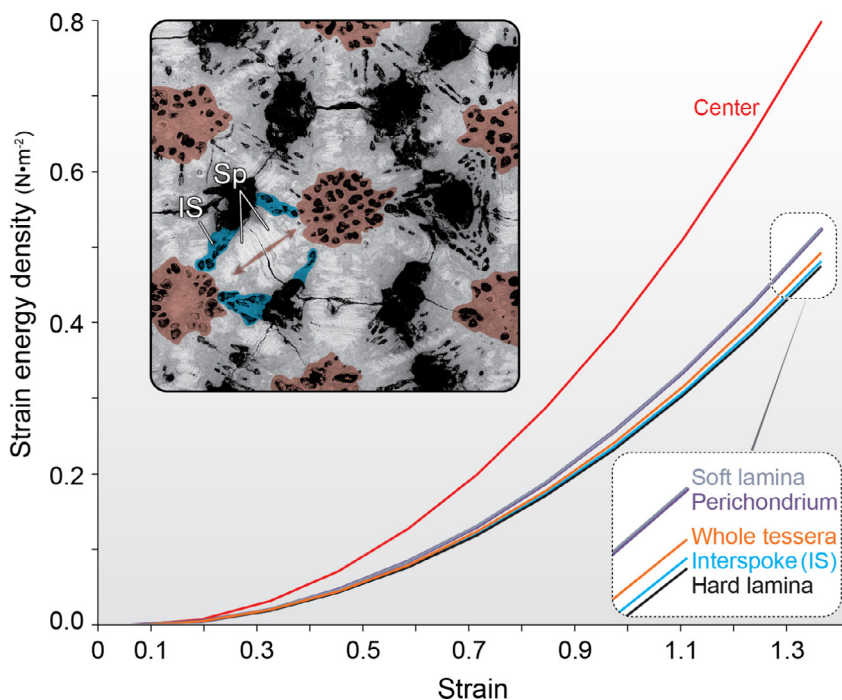


Fig. 7. Strain energy density in tesseral ultrastructural components with respect to strain. The center experiences maximum strain energy density compared to other ultrastructures. As shown in the inset backscatter electron microscopy image, the center (shaded red) is filled with cells (housed in the black lacunae shown here), which may act as mechanosensors for stresses (indicated by red arrows) ferried through spokes (Sp). The interspoke (IS) region (colored blue) is also cell-rich but is off-axis from predicted intertesseral stresses. [For interpretation of the references to color in this figure legend, the reader is referred to the web version of this article.]

neous models (i.e. models with laminated spokes), stress oscillated according to the periodicity of spoke laminations, with local maxima in high mineral density laminae (HMDL), local minima in low mineral density laminae (LMDL), and frequency increasing as the number of laminae increased (see Fig. 9). This indicates a potential protective advantage in having tesseral spoke laminae be very thin. Since spokes are the highest modulus features in tesserata (Seidel et al., 2019) and are associated with contact zones (Seidel et al., 2016), they will regularly experience high stresses, increasing their chance of material failure relative to adjacent, richly cellular ultrastructures (e.g. interspoke regions). The high frequency of stress oscillations predicted for the biological model (151 laminae, Fig. 9), however, indicates that the laminar structure of spokes may function to contain any damage resulting from a load.

Periodic material inhomogeneities (i.e. oscillating local variation in tissue structure and/or modulus) are common strategies in biological materials for reducing the driving force of cracks forming in tissue (Fratzl et al., 2016, 2007). These function to dissipate the energy of fracture, often by deflecting growing cracks at points of a sudden change in material or structural properties (e.g. weak interfaces, modulus mismatches between tissue layers) (Fratzl et al., 2016, 2007; Kolednik et al., 2011). The thin lamellae of tesseral spokes, resulting in periodic modulus variation over very small spatial scales, should increase the toughness of tesserata by increasing the predicted path length for forming cracks, and thereby the rate by which they are robbed of energy. This is supported by the zig-zagging cracks that can form in spokes during dehydration in sample preparation (see *Leucoraja* image in Fig. 4), indicating that forming radial cracks were periodically re-routed to run parallel to and not through laminae. The natural fracture behavior of tesserata, however, remains to be investigated, as does the ultrastructure of spoke laminae (particularly in 3d), which may involve additional structural means of controlling fracture energy (e.g. via the architecture of underlying fibrous material).

3.3. Global behavior of tesserata

Our global model indicates that the tesseral network could also respond flexibly to different loading scenarios at larger length scales. Stress-strain curves of in-plane loading of the tesseral mat are plotted for tension and compression regimes in Fig. 10. In tension, the joint material accommodates stress as the tesserata are pulled apart from one another (see Fig. 10A). In compression, there are two phases in the material behavior. Before tesserata coming into contact, they behave like rigid bodies squeezing the soft fibrous joints, which take all the load and undergo large deformations. Once in contact, however, the stress in the tesserata increases sharply (inset, Fig. 10B). This supports hypotheses that tesseral mats will exhibit a tension-compression asymmetry in loading, being softer in tension and stiffer in compression (Fratzl et al., 2016; Liu et al., 2014, 2010; Seidel et al., 2019). In addition, our structural variations on the base model show that the mechanical behavior of the tesseral mat can be easily tailored: increasing the size of tesseral joints delays tesseral collision to higher strains (i.e.

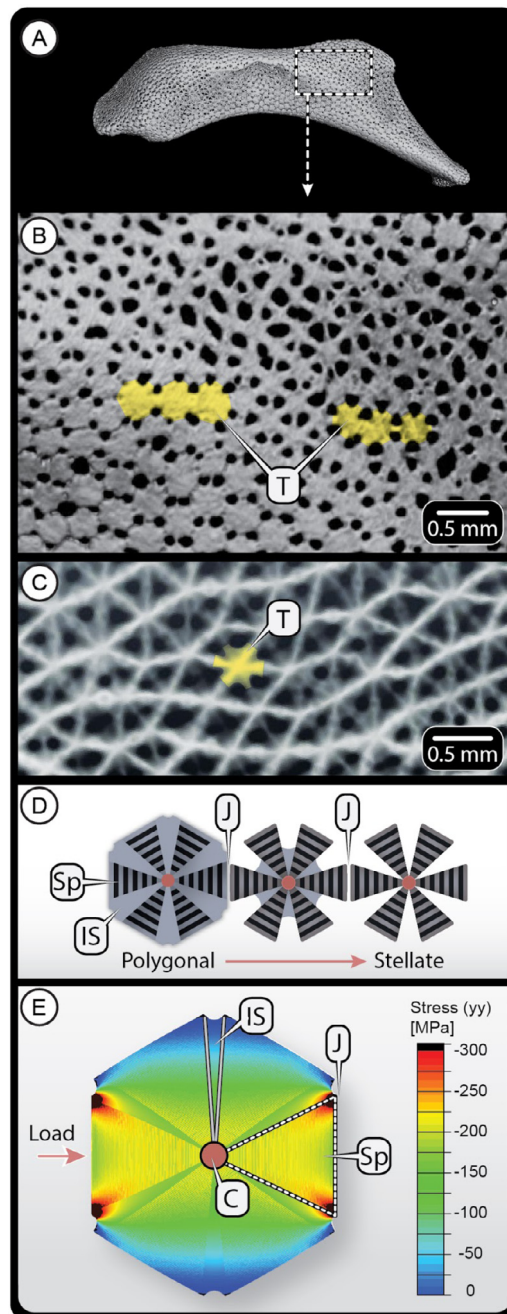


Fig. 8. Stellate tesserae. A) MicroCT of a hyomandibula (from Fig. 1B) and B) a zoomed in region, showing a gradient in tesseral shape with two sets of three exemplar tesserae (T) marked in yellow: more typical polygonal tesserae on the left and stellate tesserae on the right. C) A large region of stellate tesserae from the propterygium of *U. halleri* (microCT image). D) Schematic of the structural differences between polygonal and stellate tesserae, showing the reduction of the interspoke region (IS) and the predominance of spokes (Sp) in stellate tesserae. Note that joints (J) are located approximately midway between the centers (C) of adjacent tesserae in the microCT images in B and C, although they are not always clearly visible in microCT scans (a function of resolution being inadequate to resolve the narrow intertesseral joint spaces). E) Maximum stress in a finite element simulation, illustrating stresses passing predominantly through on-axis spokes. This renders interspoke regions largely mechanically redundant, perhaps explaining the observed morphology of stellate tesserae. [For interpretation of the references to color in this figure legend, the reader is referred to the web version of this article.]

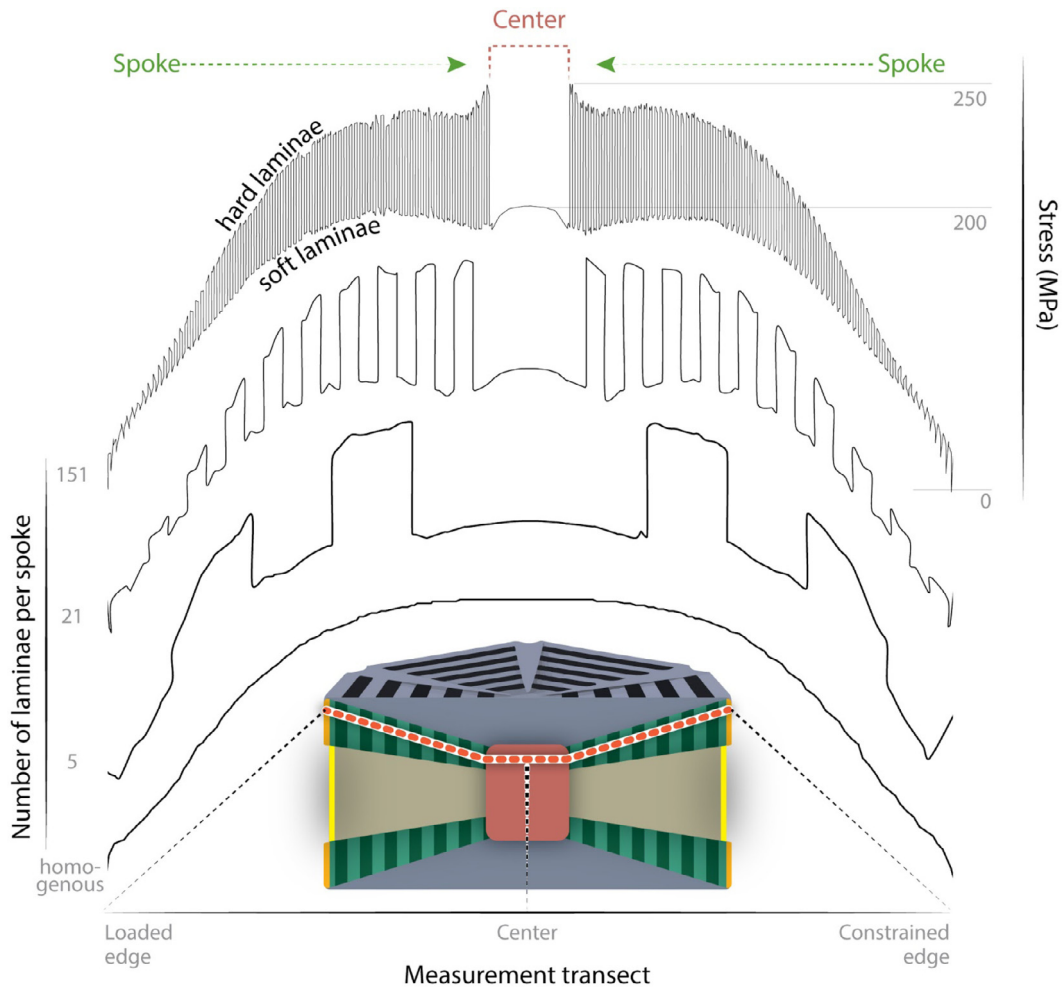


Fig. 9. Comparison of stresses along a measurement transect—from the loaded edge of the tesserella to the constrained edge, through the on-axis spokes and center—for models with increasing spoke lamina number (from bottom to top: homogeneous model, 5, 21, 151 laminae). The measurement transect is illustrated by the red dashed line on the cross-sectioned tesserella schematic at the bottom of the figure. The shape of the graphs is more relevant here than the absolute values, but the stress y-axis at the top right applies to all models: the absolute minimum is zero MPa, the stress in the center is approximately 200 MPa, and the absolute maximum is 250 MPa. Note that with increase in lamina number, the stress oscillation wavelength decreases, suggesting thinner laminae may protect tesserellae by causing cracks to follow more circuitous paths when damage evolves. [For interpretation of the references to color in this figure legend, the reader is referred to the web version of this article.]

note the shift of the curve's inflection point in Fig. 10B), whereas altering tesserella material properties changes the slope of the post-inflection curve (compare the 25 and 35 GPa models in Fig. 10B).

4. Conclusions

The parametric models designed here illustrate that the effective modulus of tesserellae and the tesserella mat is a function of specific structural and/or material properties, which could be tuned at multiple size scales in response to changing loading conditions. At the size scale of a single tesserella (i.e. the local model), ultrastructural changes that cause an increase in the volume of high mineral density features (i.e. spokes) stiffen the tesserella. Since spokes and contact zones seem to be linked (Seidel et al., 2019, 2016), this observation argues that the deposition of spoke laminae (and the concomitant effect on tesserella rigidity) is a direct response to a tesserella's loading environment. The shaping of the tesserella structure by the loading environment is also suggested by the predicted stress-leading of the spokes and the existence of stellate tesserellae, where extraneous (non-load-bearing) regions are absent. In this way, our models also suggest that the majority of tesserella ultrastructures (except spokes and joints) have functions related to biology (e.g. growth, housing of cells) rather than mechanics. Our global model indicates further tuning capability at the scale of the tesserella array, where the geometry (e.g. the distance between tesserellae) and material properties (tesserella effective modulus) can control tesserella-level properties. These results thus contend that the species-level and anatomically local variations observed in tesserella shape and ultrastruc-

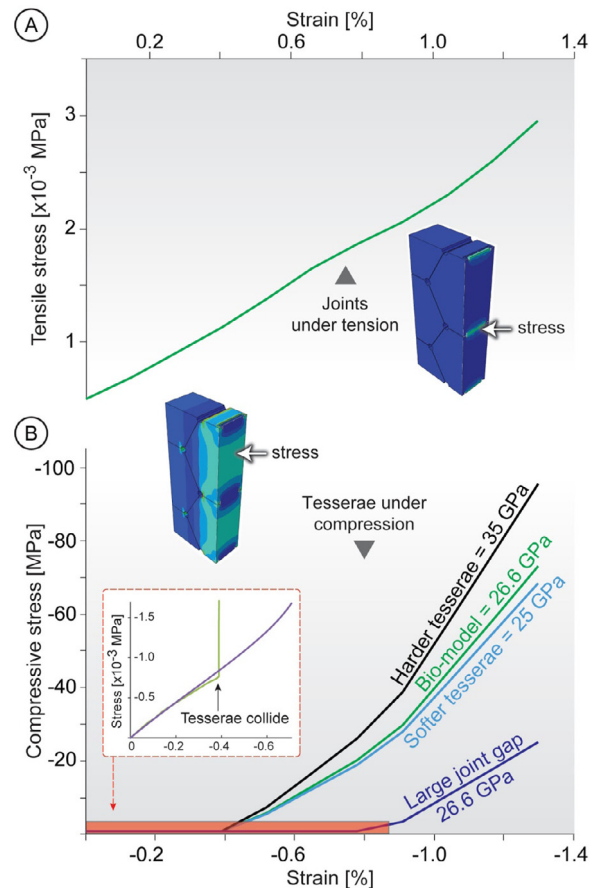


Fig. 10. Tensile and compressive stress vs. strain curves for a tessellated mat (global model). The biphasic properties of the mat—hard tiles and soft joints—result in strikingly different tensile and compressive behaviors. A) In tension, the tesserae are pulled apart and the joint material takes all the load. B) In contrast, in compression, the joint bears all the load until tesserae come into contact, inducing dramatically rising stresses. To demonstrate the tunability of the tesseral mat, three additional models are shown: with stiffer tesserae (35 GPa), with less stiff tesserae (25 GPa), and with joints 2x wider than in the base model. Note that changes in tesseral stiffness cause changes in the slope of the stress-strain curve after the tesserae-collision inflection point, whereas changes in the size of tesseral joints (distance between tesserae) shifts the position of the inflection point along the x-axis. [The reader is referred to the web version of this article, where color is used to facilitate interpretation.]

ture (Atake et al., 2019; Maisey, 2013; Seidel et al., 2016) may have distinct mechanical implications, properties that could be translated into guidelines for the bio-inspired design of tessellated materials.

Declaration of Competing Interest

None.

CRediT authorship contribution statement

A.K. Jayasankar: Conceptualization, Data curation, Formal analysis, Investigation, Methodology, Software, Validation, Visualization, Writing - original draft, Writing - review & editing. **R. Seidel:** Conceptualization, Methodology, Formal analysis, Resources, Supervision, Visualization, Writing - original draft, Writing - review & editing. **A. Hosny:** Conceptualization, Formal analysis, Methodology, Resources, Software, Supervision, Validation, Writing - review & editing. **J.C. Weaver:** Conceptualization, Funding acquisition, Methodology, Project administration, Supervision, Visualization, Writing - review & editing. **P. Fratzl:** Conceptualization, Formal analysis, Project administration, Supervision, Writing - review & editing. **J. Chen:** Conceptualization, Formal analysis, Investigation, Methodology, Project administration, Resources, Software, Supervision, Validation, Writing - original draft, Writing - review & editing. **M.N. Dean:** Conceptualization, Methodology, Formal analysis, Funding acquisition, Project administration, Resources, Supervision, Validation, Visualization, Writing - original draft, Writing - review & editing.

Acknowledgments

We would like to thank the Company of Biologists and Journal of Experimental Biology for providing the first author with a travel grant to work at the AMOLF research institute. We also thank Bas Overvelde for his hospitality at AMOLF, for his help in experimental design and for teaching the first author Python scripting for ABAQUS. Brian Eames and Joseph Atake provided useful discussion and microCT scan data to strengthen our arguments regarding stellate tesseræ and Júlia Chaumel provided the microCT image in Fig. 8C.

Funding

This work was supported by an HFSP Young Investigators Grant to MND and JCW [grant number RGY0067-2013].

Appendix

A.1. Mesh sensitivity analysis

Mesh sensitivity analysis was performed to determine the effect of seed size on average stress measured in the tesseræ models. The volume averaged stress was calculated as explained in the Methods section. When the seed size was decreased from 0.02 to 0.01 by an interval of 0.015, the volume averaged stress values changed from -148.6 to -148.3 MPa (see Fig. A.1). This 0.2% decrease in stress is acceptable for our approximations; a seed size was 0.015 used to optimize computational time.

A.2. OGDEN coefficients

The material coefficients used to model the intertesseræ joint material are listed in the table above. The properties of this material are unknown and so the material model was built by combining the stress-strain values of tendon in tension (Maganaris and Paul, 1999) and mucosa in compression (Chen et al., 2015). The coefficients for the stress-strain data were generated using the ABAQUS material editor's library of hyperelastic material models.

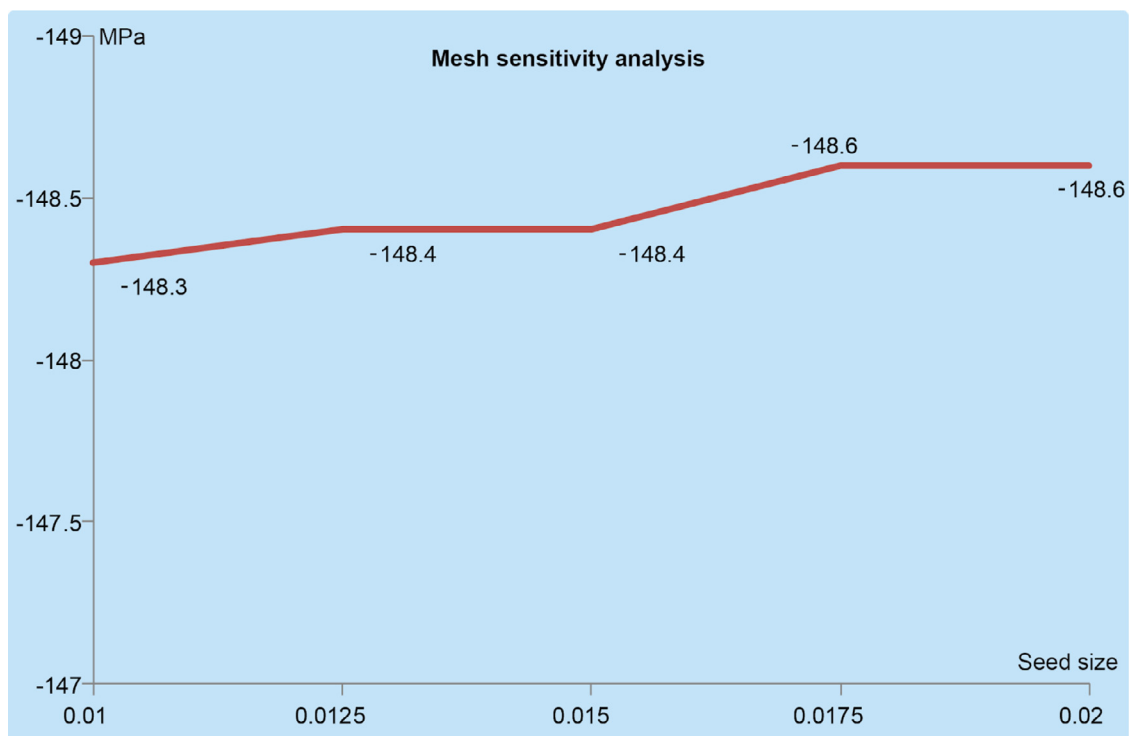


Fig. A.1. Mesh sensitivity analysis for Finite Element Analysis of tesseræ models, comparing seed size (x-axis) to stress (S_{yy} in MPa, y-axis).

Table A.2
Coefficients of Ogden 2nd order hyperelastic material model.

μ_1	α_1	μ_2	α_2	D1	D2
0.497324729	7.40136068	-0.426810081	1.76390678	2.33119738	0

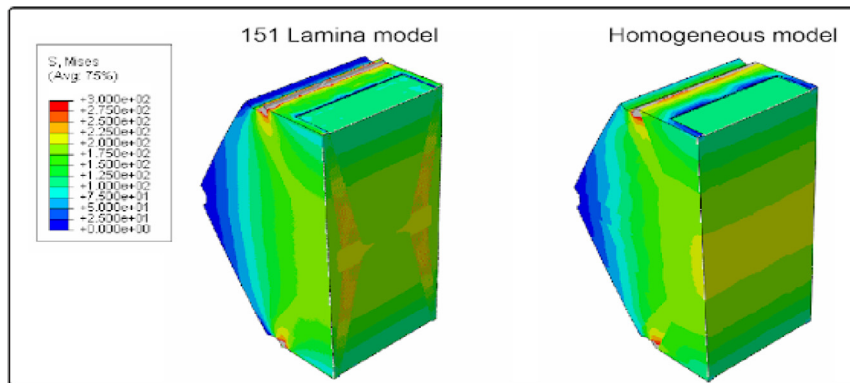


Fig. A.3. The effect of ultrastructure on Von Mises stress distribution in the 151 lamina model (left) vs. a homogeneous model lacking ultrastructure (right). There are high stresses at the center in the homogeneous model which may lead to damage of cells in the center. The spoke laminae act to transfer stress through the tessera to the center, but also act as stress sinks to protect the tessera's central region.

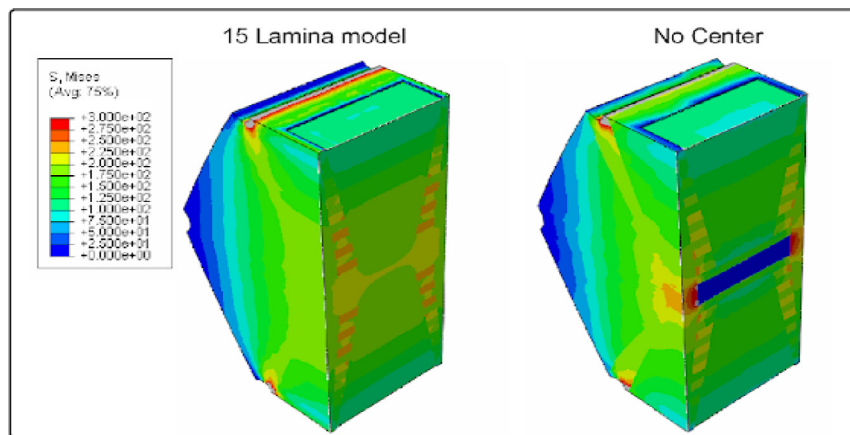


Fig. A.4. The effect of the center region on tesserae mechanics, illustrated by comparing a typical 15-lamina model (left) and a model with a negligible modulus for the center region (right). Excepting the center region itself, stress contours are largely comparable in the two models, indicating that the center plays little significance in overall tesserae mechanics.

A.3. Homogeneous (no laminae) model

As part of the experiments to understand the effect of lamina number on stress propagation in tesserae (see Fig. 9), a homogeneous tessera model (i.e. lacking ultrastructural features) was constructed as a comparison. In this model, the effective modulus calculated from the 151 lamina model (26.1 GPa) was assigned to all ultrastructural regions, thereby simulating a tessera without ultrastructure. FEA was performed as discussed in the Methods section. Whereas the homogeneous tessera does, as a function of its geometry, exhibit some radiation of stresses toward its center, it can be observed in Fig. A.3 that the homogeneous model lacks the distinct stress radiation patterns characteristic of tesserae with spokes and that the spokes apparently act as stress sinks to reduce some of the stress reaching the tesseral center.

A.4. Absence of center

To verify the effect of the center region on ultrastructural mechanics, a 15-lamina model was used and the center region was assigned a material property of ~ 0 MPa to simulate a tessera without any center. Given the integrated nature of components in model construction (see Methods) and to avoid edge effects, this method was deemed more feasible than removing the central region entirely. The calculated effective modulus of both tessera models was the same (~ 26.1 GPa),

indicating that the center plays little role in overall tesseral rigidity. Von Mises stress contours in both tesseræ were also similar, except in the perichondral and chondral regions, which bore a larger proportion of the stresses in the model lacking the central region. Fig. A.4

References

- Atake, O.J., Cooper, D.M.L., Eames, B.F., 2019. Bone-like features in skate suggest a novel elasmobranch synapomorphy and deep homology of trabecular mineralization patterns. *Acta Biomater.* 84, 424–436.
- Balaban, J.P., Summers, A.P., Wilga, C.A., 2014. Mechanical properties of the hyomandibula in four shark species. *J. Exp. Zool. A Ecol. Genet. Physiol.* 323, 1–9.
- Chen, C., Tambe, D.T., Deng, L., Yang, L., 2013. Biomechanical properties and mechanobiology of the articular chondrocyte. *Am. J. Physiol. Cell Physiol.* 305, C1202–C1208.
- Baum, D., Weaver, J.C., Zlotnikov, I., Knötel, D., Tomholt, L., Dean, M.N., 2019. High-throughput segmentation of tiled biological structures using random walk distance transforms. *Integr. Comp. Biol.* 59 (6), 1700–1712. doi:10.1093/icb/icz117.
- Chaumel, J., Schotte, M., Bizzarro, J., Zaslansky, P., Fratzl, P., Baum, D., Dean, M.N., 2020. Co-aligned chondrocytes: Zonal morphological variation and structured arrangement of cell lacunae in tessellated cartilage. *Bone*, 115264 doi:10.1016/j.bone.2020.115264, In press.
- Chen, J., Ahmad, R., Li, W., Swain, M., Li, Q., 2015. Biomechanics of oral mucosa. *J. R. Soc. Interface* 12, 20150325.
- Chen, J., Chen, L., Chang, C.-C., Zhang, Z., Li, W., Swain, M.V., Li, Q., 2017. Micro-CT based modelling for characterising injection-moulded porous titanium implants. *Int. J. Numer. Method. Biomed. Eng.* 33. doi:10.1002/cnm.2779.
- Clement, J.C., 1992. Re-examination of the fine structure of endoskeletal mineralization in chondrichthyan: implications for growth, ageing and calcium homeostasis. *Aust. J. Mar. Freshw. Res.* 43, 157–181.
- Dean, M.N., Bizzarro, J.J., Clark, B., Underwood, C.J., Johanson, Z., 2017. Large batoid fishes frequently consume stingrays despite skeletal damage. *R. Soc. Open Sci.* 4 170674–170611.
- Dean, M.N., Ekstrom, L., Monsonogo-Ornan, E., Ballantyne, J., Witten, P.E., Riley, C., Habraken, W., Omelon, S., 2015. Mineral homeostasis and regulation of mineralization processes in the skeletons of sharks, rays and relatives (Elasmobranchii). *Semin. Cell Dev. Biol.* 46, 51–67.
- Dean, M.N., Mull, C.G., Gorb, S.N., Summers, A.P., 2009. Ontogeny of the tessellated skeleton: insight from the skeletal growth of the round stingray *Urolophus halleri*. *J. Anat.* 215, 227–239.
- Dean, M.N., Socha, J.J., Hall, B.K., Summers, A.P., 2010. Canaliculi in the tessellated skeleton of cartilaginous fishes. *J. Appl. Ichthyol.* 26, 263–267.
- Dingerkus, G., Seret, B., 1991. Multiple prismatic calcium phosphate layers in the jaws of present-day sharks (Chondrichthyes; selachii). *Experientia* 47, 38–40.
- Ferrara, T.L., Clausen, P., Huber, D.R., McHenry, C.R., Peddemors, V., Wroe, S., 2011. Mechanics of biting in great white and sandtiger sharks. *J. Biomech.* 44, 430–435.
- Fratzl, P., Gupta, H.S., Fischer, F.D., Kolednik, O., 2007. Hindered crack propagation in materials with periodically varying Young's modulus—Lessons from biological materials. *Adv. Mater.* 19, 2657–2661.
- Fratzl, P., Kolednik, O., Fischer, F.D., Dean, M.N., 2016. The mechanics of tessellations - bioinspired strategies for fracture resistance. *Chem. Soc. Rev.* 45, 252–267.
- Jayasankar, A.K., Seidel, R., Naumann, J., Guiducci, L., Hosny, A., Fratzl, P., Weaver, J.C., Dunlop, J.W.C., Dean, M.N., 2017. Mechanical behavior of idealized, stingray-skeleton-inspired tiled composites as a function of geometry and material properties. *J. Mech. Behav. Biomed. Mater.* 73, 86–101.
- Kemp, N., Westrin, S.K., 1979. Ultrastructure of calcified cartilage in the endoskeletal tesseræ of sharks. *J. Morphol.* 160, 75–101.
- Knötel, D., Seidel, R., Prohaska, S., Dean, M.N., Baum, D., 2017. Automated segmentation of complex patterns in biological tissues: lessons from stingray tessellated cartilage. *PLoS ONE* 12, e0188018–e0188024.
- Kolednik, O., Predan, J., Fischer, F.D., Fratzl, P., 2011. Bioinspired design criteria for damage-resistant materials with periodically varying microstructure. *Adv. Funct. Mater.* 21, 3634–3641.
- Lammi, M.J., 2004. Current perspectives on cartilage and chondrocyte mechanobiology. *Biorheology* 41, 593–596.
- Leydig, F., 1857. *Lehrbuch der Histologie des Menschen und der Thiere*. Meidinger, Frankfurt a.M., pp. 551–pp.
- Liu, X., Dean, M.N., Summers, A.P., Earthman, J.C., 2010. Composite model of the shark's skeleton in bending: a novel architecture for biomimetic design of functional compression bias. *Mater. Sci. Eng. C* 30, 1077–1084.
- Liu, X., Dean, M.N., Youssefpoor, H., Summers, A.P., Earthman, J.C., 2014. Stress relaxation behavior of tessellated cartilage from the jaws of blue sharks. *J. Mech. Behav. Biomed. Mater.* 29, 68–80.
- Macesic, L.J., Summers, A.P., 2012. Flexural stiffness and composition of the batoid propterygium as predictors of punting ability. *J. Exp. Biol.* 215, 2003–2012.
- Maganaris, C.N., Paul, J.P., 1999. In vivo human tendon mechanical properties. *J. Physiol.* 521 (Pt 1), 307–313.
- Maisey, J.G., 2013. The diversity of tessellated calcification in modern and extinct chondrichthyan. *Revue de Paléobiologie, Genève* 32, 355–371.
- Petrie, C.S., Williams, J.L., 2005. Comparative evaluation of implant designs: influence of diameter, length, and taper on strains in the alveolar crest. a three-dimensional finite-element analysis. *Clin. Oral Implants Res.* 16, 486–494.
- Roth, W., 1911. Beiträge zur Kenntnis der Strukturverhältnisse des Selachierknorpels. *Morphologisches Jahrbuch* 42, 486–555.
- Seidel, R., Blumer, M., Pechrigg, E.-J., Lyons, K., Hall, B.K., Fratzl, P., Weaver, J.C., Dean, M.N., 2017a. Calcified cartilage or bone? Collagens in the tessellated endoskeletons of cartilaginous fish (sharks and rays). *J. Struct. Biol.* 200, 54–71.
- Seidel, R., Blumer, M., Zaslansky, P., Knötel, D., Huber, D.R., Weaver, J.C., Fratzl, P., Omelon, S., Bertinetti, L., Dean, M.N., 2017b. Ultrastructural, material and crystallographic description of endophytic masses—a possible damage response in shark and ray tessellated calcified cartilage. *J. Struct. Biol.* 198, 5–18.
- Seidel, R., Jayasankar, A.K., Shahar, R., Dean, M.N., 2019a. The multiscale architectures of fish bone and tessellated cartilage and their relation to function. In: Estrin, Y., Bréchet, Y., Dunlop, J., Fratzl, P. (Eds.), *Architected Materials in Nature and Engineering*. Springer Series in Materials Science, pp. 329–353.
- Seidel, R., Lyons, K., Blumer, M., Zaslansky, P., Fratzl, P., Weaver, J.C., Dean, M.N., 2016. Ultrastructural and developmental features of the tessellated endoskeleton of elasmobranchs (sharks and rays). *J. Anat.* 229, 681–702.
- Seidel, R., Roschger, A., Li, L., Zhang, Q., Yin, J., Yang, T., Weaver, J.C., Fratzl, P., Roschger, P., Dean, M.N., 2019b. Mechanical properties of stingray tesseræ: high-resolution correlative analysis of mineral density and indentation moduli in tessellated cartilage. *Acta Biomater.* 96, 421–435. doi:10.1016/j.actbio.2019.06.038.
- Sih, G.C., Macdonald, B., 1974. Fracture mechanics applied to engineering problems-strain energy density fracture criterion. *Eng. Fract. Mech.* 6, 361–386.
- Summers, A.P., 2000. Stiffening the stingray skeleton—an investigation of durophagy in myliobatid stingrays (Chondrichthyes, Batoidea, Myliobatidae). *J. Morphol.* 243, 113–126.
- Summers, A.P., Ketcham, R., Rowe, T., 2004. Structure and function of the horn shark (*Heterodontus francisi*) cranium through ontogeny—the development of a hard prey specialist. *J. Morphol.* 260, 1–12.
- Wann, A.K.T., Zuo, N., Haycraft, C.J., Jensen, C.G., Poole, C.A., McGlashan, S.R., Knight, M.M., 2012. Primary cilia mediate mechanotransduction through control of ATP-induced Ca²⁺ signaling in compressed chondrocytes. *FASEB J.* 26, 1663–1671.
- Wegst, U.G.K., Ashby, M.F., 2004. The mechanical efficiency of natural materials. *Philos. Mag.* 84, 2167–2186.
- Wilga, C.A.D., Diniz, S.E., Steele, P.R., Sudario-Cook, J., Dumont, E.R., Ferry, L.A., 2016. Ontogeny of feeding mechanics in smoothhound sharks: morphology and cartilage stiffness. *Integr. Comp. Biol.* 56, 442–448.

- Wroe, S., Huber, D.R., Lowry, M., McHenry, C., Moreno, K., Clausen, P., Ferrara, T.L., Cunningham, E., Dean, M.N., Summers, A.P., 2008. Three-dimensional computer analysis of white shark jaw mechanics: how hard can a great white bite? *J. Zool.* 276, 336–342.
- Wu, Q.Q., Chen, Q., 2000. Mechanoregulation of chondrocyte proliferation, maturation, and hypertrophy: ion-channel dependent transduction of matrix deformation signals. *Exp. Cell Res.* 256, 383–391.
- Zhang, W., Soman, P., Meggs, K., Qu, X., Chen, S., 2013. Tuning the Poisson's ratio of biomaterials for investigating cellular response. *Adv. Funct. Mater.* 23. doi:10.1002/adfm.201202666.